Proceedings of the ASME 2022 17th International Manufacturing Science and Engineering Conference MSEC2022 June 27-July1, 2022, West Lafayette, Indiana, USA

MSEC2022-85633

UNEXPECTEDLY HIGH YIELDS IN CHEMICAL VAPOR DEPOSITION OF CARBON NANOTUBES BASED ON REACTOR WALL THERMOCHEMICAL HISTORY

Golnaz Tomaraei

Department of Industrial Engineering
University of Pittsburgh
Pittsburgh, PA, USA

Moataz Abdulhafez

Department of Industrial Engineering University of Pittsburgh Pittsburgh, PA, USA

Mostafa Bedewy*

Department of Industrial Engineering, Department of Chemical and Petroleum Engineering, Department of Mechanical Engineering and Materials Science
University of Pittsburgh, Pittsburgh, PA, USA
*mbedewy@pitt.edu

ABSTRACT

While reactor wall preconditioning was previously shown to influence the growth of carbon nanotubes (CNTs) by chemical vapor deposition (CVD), it was previously only limited to studying the accumulating carbon deposits over the history of a large number of growth runs. However, the effect of leaving the reactor walls for an extended period of time between growth runs was not previously systematically studied. Here, we combine experimental measurements with a mathematical model to investigate the effect of thermochemical history of reactor walls on growth yield of vertically aligned CNT forests. Importantly, we demonstrate unexpectedly high CNT yield, exceeding oneorder-of-magnitude taller forests, by increasing the interim period between runs (IPBR). We explain the results based on previously unexplored process sensitivity to trace amounts of oxygen-containing species in the reactor. In particular, uncontrolled amounts of water vapor desorbing from reactor walls during growth are modelled in this work. Our modeling results show the effect of IPBR on the outgassing dynamics revealing the underlying mechanism of generating growth promoting molecules during growth. By installing a new humidity sensor in our multizone rapid thermal CVD reactor, we are able to uniquely correlate the amount of moisture within the reactor to real-time measurements of growth kinetics, as well as ex situ characterization of CNT alignment and atomic defects. Our findings enable a scientifically grounded approach toward both boosting growth yield and improving its consistency by reducing run-to-run variations. Accordingly, engineered growth recipes can be envisioned to leverage this effect for improving manufacturing process scalability and robustness.

1. INTRODUCTION

Vertically aligned carbon nanotube (VACNT) forests are hierarchical macroscale structures with unique anisotropic energy and mass transport properties, as well as excellent thermal, electrical, and mechanical properties that result from both the properties of individual CNTs, as well as their collective properties that emerge from aligning billions of CNTs per square centimeter. Therefore, they possess great potential as interfacial materials for many applications including thermal interfaces [1], separation membranes [2], electrical interconnects [3], and structural fibers [4].

The growth process of VACNT forests from substrate bound catalyst nanoparticles by CVD involves several atomic scale processes that control the formation and self-organization of carbon atoms on the surface of catalyst nanoparticles to form CNTs during early stages of growth [5]. These mechanically coupled CNTs can maintain their highly aligned morphology until the final height is achieved at growth self-termination [6-9]. This early termination of growth is undesirable, because the synthesis of longer VACNTs is needed for better performance in many applications such as structural CNT fibers and varns [10]. Although methods to increase catalytic lifetime have been proposed, such as by using water vapor as additive during growth or by designing/pretreating the catalyst [11-15], this issue of limited yield remains a challenge. This is especially important considering the energy-intensive nature of the process and the negative environmental impact of CVD reactors [16]. Another roadblock toward precision growth of tailored CNT ensembles is the issue of reproducibility and run-to-run variations.

One root cause of both above-mentioned challenges is the coupling problem in typical CVD reactors such as a hot-walled tube furnace. Our approach to resolve this issue is a custom-designed multizone rapid thermal CVD reactor, which enables us to independently control the temperatures of the main steps of catalytic CVD process, namely gas-phase decomposition temperature (T_p), catalyst formation temperature (T_c), and CNT nucleation and growth temperature (T_g). Previous works in our group show that our custom-designed CVD reactor enables the investigation of previously inaccessible combination of process parameters, and thus is capable of boosting catalytic lifetime [14] and improving growth process consistency [17].

These improvements notwithstanding, the persistent issue of reproducibility has another root cause that is more difficult to control, which is the presence of small amounts of gaseous species in the reactor during growth. Indeed, the sensitivity of the growth process to uncontrolled, trace amounts of oxygencontaining molecules such as water vapor in the reactor has been shown to influence the growth process greatly contributing to run-to-run variations and lower growth yields [17–20]. Accordingly, we have previously proposed scientifically grounded approaches toward achieving statistically significant reduction in the observed run-to-run variations based on modifications to both the reactor design [21] and dynamic recipes [17].

Despite these efforts, the condition of reactor wall is still a largely unexplored source of variation. In particular, the effect of the thermochemical history of the reactor wall on growth consistency and yield has not been fully elucidated. Previous studies show that the accumulation of carbon deposits on reactor wall over several growth runs improves the density and uniformity of growth process, mainly due to uncontrolled presence of activated species in these carbon deposits [18,22]. Here we do a systematic study on the effect of thermochemical history of reactor wall on growth by isolating an important factor that is often overlooked in previous work. This factor is the time elapsing between growth runs, i.e. the time between the end of a growth run and the start of the following growth run in the same

reactor. In this paper, we refer to this as the interim period between runs, or IPBR for short. We show that IPBR is key for tuning the amount of water vapor molecules on the surface and within the thickness of reactor wall, which greatly influences growth. Experimental results combined with mathematical models of diffusion reveals this previously unexplored mechanism of controlling the outgassing rate of water vapor molecules from the reactor wall during growth and its impact on the yield and uniformity of CNT forests.

2. MATERIALS AND METHODS

2.1 Sample preparation

A 4-inch Si (001) wafer with a 300-nm thick SiO_2 layer was coated with a 10 nm thick alumina layer and a 1-nm thick Fe catalyst film on top of alumina in the same deposition run using sputtering. The catalyst-coated wafer was then diced into samples of 10 mm \times 10 mm. The samples were placed on the 50 μ m-deep recessed area at the center of a 2-inch Si wafer (substrate support wafer) and loaded into the multizone rapid thermal processing (RTP) CVD reactor.

2.2 Multizone RTP-CVD reactor

Fig. 1 shows a schematic of our multizone RTP-CVD reactor. A detailed description of the reactor can be found in the previous studies of our group [23,24]. The reactor has been designed to overcome the coupling issue of temperatures during the three separate process steps of gas-phase decomposition, catalyst preparation, and CNT nucleation/growth. Instead of a single slow-heating zone in most typical hot-walled reactors, our reactor consists of a resistive preheater for gas-phase reactions and an infrared (IR) furnace adjacent to the preheater to achieve high heating rates during catalyst formation and CNT growth steps. The twelve halogen lamps making up the IR furnace are divided up into three zones along the axis of the reactor. Moreover, the six lamps at the top and the six at bottom are independently controlled. Accordingly, this reactor design uniquely enables creating automatic dynamic recipes with engineered spatiotemporal gradients of temperature.

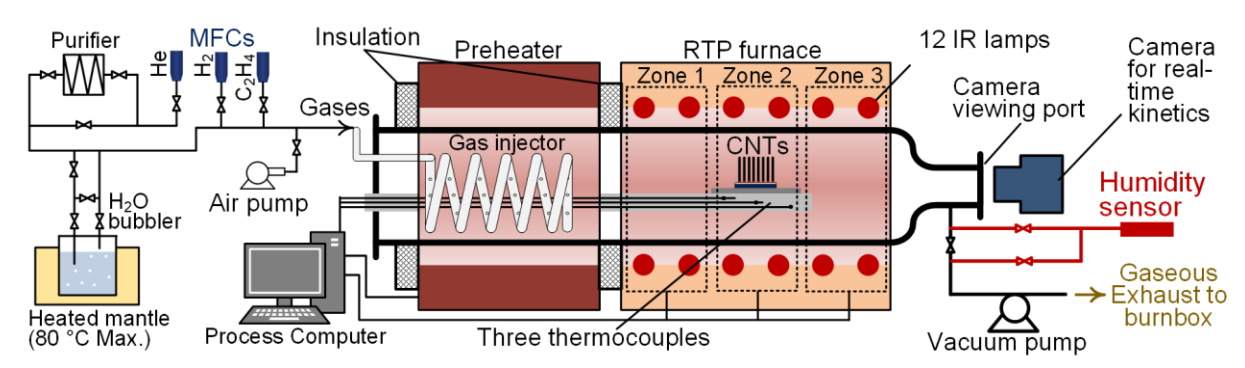


FIGURE 1: Schematic representation of the custom-designed rapid thermal CVD reactor which shows the newly installed humidity sensor.

The delivery and flow rate of process gases are controlled by a system of mass flow controllers. Additionally, a bubbler with controllable pressure and temperature is used to deliver the desired flow of water vapor molecules. A viewing port into the reaction chamber allows real time monitoring of the process using videography. The growth process of each CNT forest is recorded by a high magnification CCD camera. Image processing is used to plot the time evolution of forest height, i.e. height kinetics, from which growth rates and catalytic lifetimes are calculated [23].

2.3 CNT forest growth recipes

Before every CNT growth experiment, we run an air baking step according to the recipe shown in Fig. 2. During this step, all three zones are heated to 1000 °C in air and stay at this temperature for 25 minutes in order to burn off the carbon deposits on the reactor wall, remaining from a previous run. Each baking recipe ends with a vacuum pumping to below 30 mTorr followed by a helium purge. The substrate holder is kept inside the RTP furnace during baking, but the sample is loaded only when the reactor is cooled down to below 80 °C.

A typical growth recipe can be seen in Fig. 2. Each growth recipe starts with a long room temperature vacuum pumping step. Here, a recipe with $T_c = T_g = 700\,^{\circ}\text{C}$ was used to grow CNT forests. The total flow rate during both catalyst formation and growth steps was 1700 SCCM. During catalyst formation step, 490 SCCM H_2 and 200 SCCM of He through the water bubbler was used and the rest of the flow was dry He. During the growth step, 370 SCCM of He was replaced by gaseous carbon feed, namely 365 SCCM C_2H_4 and 5 SCCM C_2H_2 . When the growth recipe ends, the reactor is cooled down to below 80 °C before it is opened, and the sample is taken out.

Helium purge step after growth. Finally, a room temperature vacuum pumping to below 30 mTorr followed by a helium purging step is performed until the pressure reaches atmospheric pressure. The reactor is kept under atmospheric pressure during the IPBR until the process is repeated with the next growth run. The sequence of the events described above is schematically illustrated in Fig. 2.

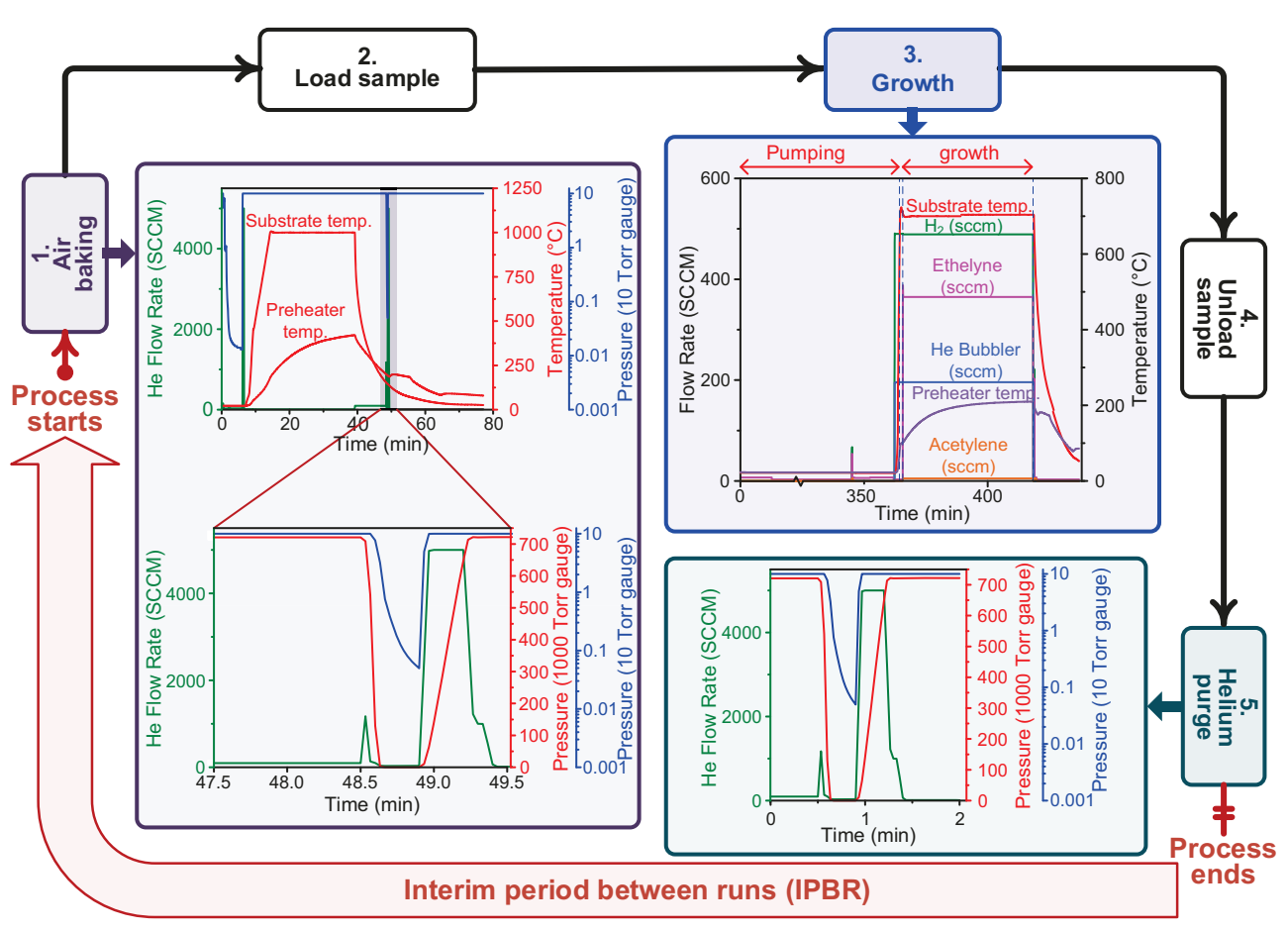


FIGURE 2: Schematic representation of the sequence of steps taken within each growth run in our CVD reactor, along with IPBR between two consecutive growth runs. Time evolution of the process gases as well as the pressures are plotted for the recipes used for each of the three steps of air baking, growth, and helium purge steps.

2.4 Characterization of CNT forests

Optical images of the sides of each forest were used to determine the height. The morphology of the as-grown CNT forests was analyzed by scanning electron microscopy (SEM) at the bottom and top of the side walls of CNT forests, using JEOL JSM-6510. The structural quality of CNT forests was assessed by a Renishaw inVia Raman spectrometer using a laser with 633 nm excitation wavelength.

2.5 Installing humidity sensor

As the schematic in Fig. 1 illustrates, in this study the gas outlet plumbing was reconfigured to add a humidity sensor to our custom-designed CVD reactor. A set of valves are used to modulate when the flow of exhaust gases coming out of the reactor is allowed into the hygrometer by-pass. The humidity sensor is integrated into the system during the room temperature vacuum pumping at the beginning of the growth recipes before IR heating starts. The flow of hot gas into the hygrometer is stopped by closing the pneumatic valves to avoid any damage to the sensor due to exposure to high temperatures or to hydrocarbon decomposition by-products.

2.6 Mathematical modeling

To complement our experimental measurements, we utilized mathematical models that describe the time-dependent diffusion of water vapor molecules into fused silica, and we combined them with the existing mathematical formulas for outgassing of water vapor molecules from the reactor walls via diffusion and desorption during vacuum pumping [25]. We use these models to further investigate the effect of IPBR on the water vapor amount that is outgassed from the reactor wall during the growth process and correlate it to the yield, uniformity, and properties of CNT forests.

3. RESULTS AND DISCUSSION

3.1 Experimental CNT forest characterization

CNT forests were grown with the same growth recipe but different IPBRs. As seen in Fig. 3, the optical images from the side view of the forests reveal significant increase in the height of the forests grown after a long IPBR (90 days). Additionally, these forests often show considerable geometric nonuniformities compared to the ones grown after a short IPBR (1 day). Lowmagnification SEM images of two CNT forests with 1-day and 90-day IPBR are provided in Fig. 4 to better illustrate the difference in size and geometries between the two forests. The nonuniformities observed in Fig. 4c and 4d for the forest with 90-day IPBR are explained by the switch in growth rates observed during growth from the videography and plotted kinetics in Fig. 3a. Internal stresses develop during growth because of growth rate mismatch between individual nanotubes [26-29]. These stresses magnify in taller forests with longer catalytic lifetime, leading to cracking and having parts of the forest growing taller than other parts. These macroscale (cmscale), stress-induced geometric nonuniformities have been previously shown to arise from both mechanical and chemical coupling between neighboring CNTs that grow simultaneously at different rates [26–28]. As shown in the height kinetics curves in Fig. 3a, it is observed that while the initial growth rate stays almost unaffected, catalytic lifetime increases significantly for the longer IPBR.

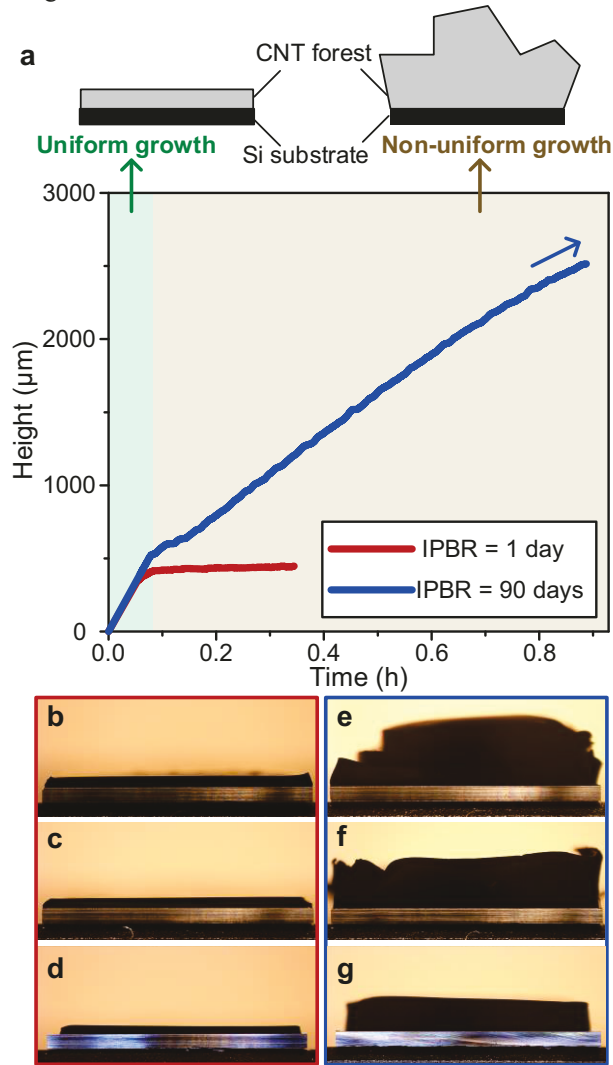


FIGURE 3: (a) *In situ* growth kinetics curves for two forests with 1-day and 90-day IPBR. (b-g) Optical images of the side walls of CNT forests grown with various IPBR: (b, c, d) 1-day. (e) 90-day, (f) 51-day, and (g) 41-day.

Mechanism of increased yield for longer IPBR. It has been previously reported that an appropriate amount of water vapor increases the catalytic lifetime and CNT yield [11,30]. Therefore, a boost in catalytic lifetime can be attributed to an additional supply of water vapor molecules during growth after a long IPBR. It is worth noting that the initial green shaded area in Fig. 3a highlights the uniform growth of a CNT forest as a uniform cuboidal block with a linear growth rate, while the gold shaded area represents the transition from uniform to nonuniform geometry, concomitant with the observed kink in the height kinetics curve. The blue arrow in Fig. 3a shows that the growth was not self-terminated, i.e. the experiment was

intentionally stopped after about an hour of growth. Hence, actual catalytic lifetime is higher than that, indicating that the boost in catalytic lifetime exceeds one order of magnitude (i.e. from ~6 minutes to >60 minutes).

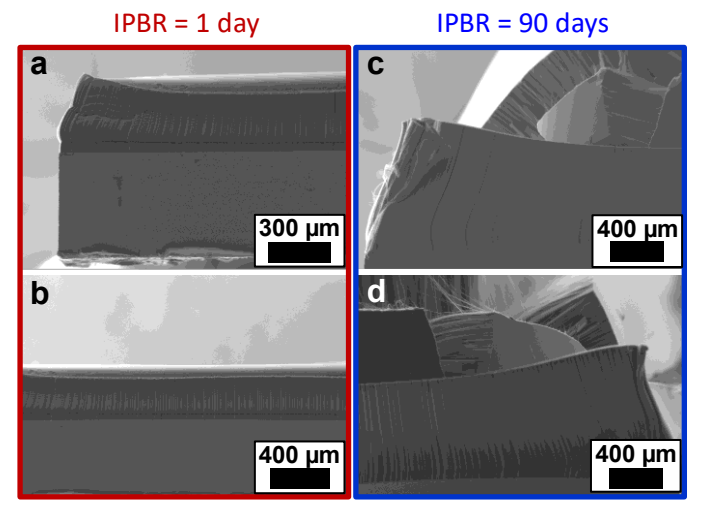


FIGURE 4: SEM images of the side walls of forests with (a,b) 1-day and (c,d) 90-day IPBR, showing the geometric nonuniformity observed with longer IPBR.

To characterize CNT crystallinity and atomic structure, Raman spectra were collected from three points on the top surface of each CNT forest. Representative spectra for each forest are shown in Fig. 5a. To investigate the structural quality of CNTs, the average ratio between G-band and D-band (I_G/I_D) was calculated for each forest from three spectra. Fig. 5b demonstrates the effect of IPBR on the average I_G/I_D ratios. Results show that in all cases the quality of CNTs grown with different IPBRs is good with slight decrease in the average I_G/I_D value for forests with extended IPBR. This small difference is explained due to the accumulation of amorphous carbon on the top surface during longer growth times [31].

Figure 6 shows the high-magnification SEM images from the sidewalls of two forests with 1-day and 90-day IPBR. These sidewall images were obtained from near the top and near the bottom of the forests. Both forests exhibit relatively good alignment and density, with better alignment near the top, compared the bottom. These results are consistent with previous work elucidating the collective nature of CNT forest growth [6,7]. However, the taller forest grown with 90-day IPBR has slightly lower alignment at the bottom (corresponding to the end stage of growth) and slightly lower density at the top.

3.2 Humidity measurements

To verify the effect of IPBR on the dynamics of reactor wall outgassing and the amount of water vapor desorbing from the wall surface, we installed a humidity sensor, as shown in the bottom right corner of Fig. 1. The change in moisture level during the growth recipe for CNT forests grown after 1-day and

90-day IPBR are shown in Fig. 7. The semilogarithmic plots with base-10 logarithmic scale for x axis and linear scale for v axis are included in Fig. 7c and 7d (for 1-day and 90-day IPBR, respectively) to better show the changes in moisture content during vacuum pumping and growth steps. As shown in Fig. 7. extended IPBR leads to a significant increase in the moisture content at the beginning of the growth recipe although an air baking recipe preceded both growth experiments. This finding indicates that the longer reactor walls are left at atmospheric pressure in-between runs, the higher the water vapor content in the reactor during pumping and growth. These results explain the boost in catalytic lifetime observed from *in-situ* kinetics curves of these two forests shown in Fig. 3a. As mentioned earlier, the reactor exhaust gases are routed through humidity sensor only during the room temperature vacuum pumping step prior to growth, i.e. before IR heating starts. Accordingly, the increase in the moisture content during the growth stage shown in Fig. 7 for the forest with 90-day IPBR confirms that the humidity level in

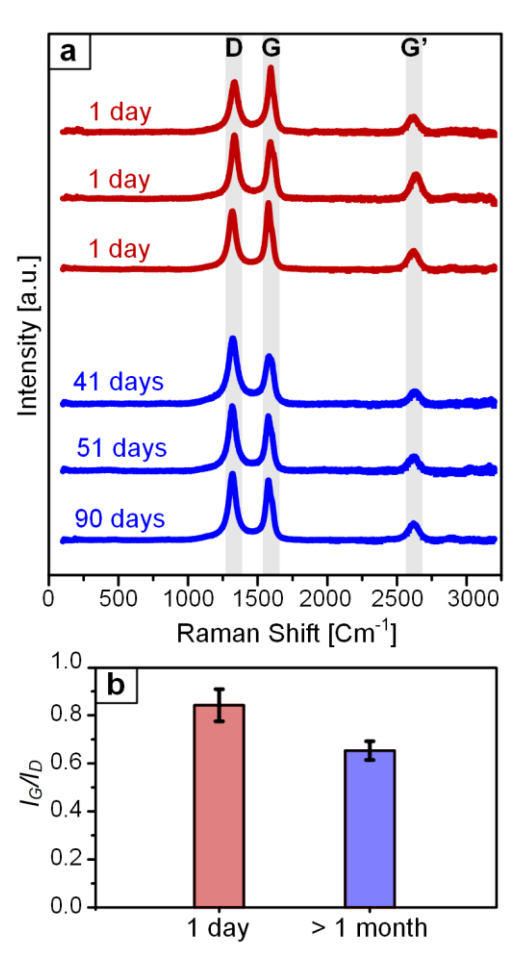


FIGURE 5: Effect of IPBR on the structural quality of CNTs. (a) Raman spectra collected from the top of CNT forests grown after different IPBRs. (b) I_G/I_D ratios with error bars obtained from three measurements on three forests grown in separate runs. The average I_G/I_D value for > 1 month was obtained from three forests with 41-, 51-, and 90-day IPBR.

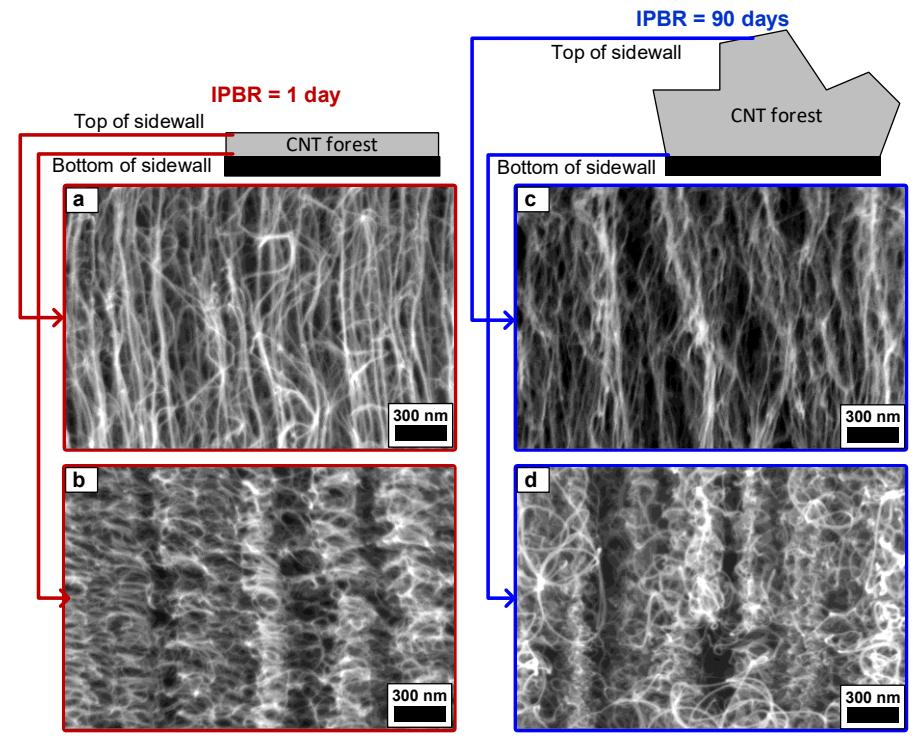


FIGURE 6: H-magnification SEM images of the side walls of forests near the top and bottom for 1-day IPBR (a,b) and 90-day IPBR (c,d).

the reactor is dominated by the outgassing of water vapor molecules from all internal walls of the reactor and plumbing system. Hence, the observed trends from humidity measurements support the hypothesis that higher amounts of growth promoting molecules are desorbed from the reactor wall during the growth run after an extended IPBR.

3.3 Mathematical modeling

Here we combine our experimental measurements with mathematical models of diffusion and outgassing of water vapor molecules to further explain the mechanism underlying how higher CNT yields are achieved after longer IPBR, resulting from higher levels of water vapor desorbed from the reactor wall during the growth run.

Due to small diffusion coefficient of water vapor molecules into silica glass at low temperatures, most of previous reports are at high temperatures [32]. Oehler *et al.* [33] quantified the diffusion coefficient of water molecules into amorphous silica glass after exposure to saturated water vapor at a relatively low temperature of 250 °C for various periods of time (24 hours to 576 hours). Using IR spectroscopy to measure the absorbance values after successive etching of the surface layer to various depths, they obtain experimental concentration depth (x) profiles after various exposure times (t). These experimental profiles are fit by comparing with the theoretical profile given by Equation 1 to obtain the surface concentration, C_s , and the effective diffusion coefficient, D_{eff} of water in silica glass.

$$C(d,t) = C_s[erfc\left(\frac{x}{2\sqrt{D_{eff}t}}\right)] \tag{1}$$

Oehler *et al.* also used an alternative method of measuring water uptake, M_t , at various exposure times to determine D_{eff} values, according to Equation 2, where M_t and C_s are experimentally determined. Both methods yield similar values within the experimental error range [33].

$$M_t = 2C_s(\sqrt{\frac{D_{eff}}{\pi}})\sqrt{t}$$
 (2)

Here, we use the theoretical concentration depth profile (Equation 1) along with the C_s and $D_{\rm eff}$ values at various times provided by Oehler *et al.* [33] to replot these concentration depth profiles at various exposure times in Fig. 8. It should be noted that the values used for C_s and $D_{\rm eff}$ at 24 h and 576 h were obtained from the water uptake method, while the rest were based on fitting with theoretical profile [33].

At each exposure time, we calculate the diffusion depth, d, at which the concentration reaches 1% of C_s , and plot it as a function of time in Fig. 9a. It is observed that the data fits a power-law distribution ($d=13.31t^{0.29}$, corresponding to the dashed blue line in Fig. 9a). We also calculate the average concentration of water molecules inside silica glass within this diffusion depth as a function of exposure time by integrating the curves in Fig. 8 from surface to the depth at which the concentration is 1% of C_s . Fig. 9b shows that the average

concentration of water molecules also follows a power law distribution ($C_{avg.}=0.024t^{0.27}$, shown with dashed blue line in Fig. 9b). The dependence of $D_{\rm eff}$ on exposure time based on the results of Oehler et~al. [33] is shown in Fig. 9c, and can be expressed as a power law ($D_{eff}=3.79\times10^{-11}t^{-0.42}$, shown with dashed blue line in Fig. 9c). To elaborate on the observed power law dependence of d and $C_{avg.}$ on t, we consider Equation 1 with $C(d,t)=0.01C_s$. It follows that the term inside the complementary error function (erfc) must be a constant value, and thus $d\propto\sqrt{D_{eff}t}$. Given that $D_{eff}\propto t^{-0.42}$, it follows that $d\propto t^{(1-0.42)/2}$, i.e. $d\propto t^{0.29}$, which is in accordance with our data modeling results. Considering the integral of the erfc function as $\int_0^\infty erfc~(ax)=\frac{1}{a\sqrt{\pi}}$, $|arg~a|<\frac{\pi}{4}$, it follows that the integration of the curves in Fig. 8 gives us $\int_0^\infty C_s \left[erfc\left(\frac{x}{2\sqrt{D_{eff}t}}\right)\right] \propto 2\sqrt{\frac{D_{eff}t}{\pi}}$, and thus $C_{avg.}\propto \frac{2}{x_{\infty}}\sqrt{\frac{D_{eff}t}{\pi}} \propto t^{(1-0.42)/2} \propto t^{0.29}$, which agrees with our model.

We use the fits to estimate d and C_{avg} at various IPBR. We obtain $d_1 = 33.56 \, \mu m$ and $C_{avg,,1} = 0.057 \, mole/L$ of SiO₂ for 1-day IPBR, and $d_2 = 124.31 \, \mu m$ and $C_{avg,,2} = 0.195 \, mole/L$ of SiO₂, for 90-day IPBR. The difference between these two cases is schematically illustrated in Fig. 10b. Although these values are obtained based on available experimental data at 250 °C, at room temperature with a lower diffusion coefficient the ratio between d_1 and d_2 as well as the ratio between $C_{avg,,1}$ and $C_{avg,,2}$ should stay the same.

Water vapor molecules leave the reactor walls under vacuum through several pathways, most important of which are diffusion to the wall's surface from near-surface region and desorption from the surface [25]. The kinetics of desorption becomes much slower when there is less than a monolayer of adsorbed molecules on the surface compared to when there are multilayers of adsorbed molecules. These two pathways (schematically demonstrated in Fig. 10a) both contribute to the overall outgassing. The outgassing rate is given by:

$$q = C_0 \left(\frac{D}{nt}\right)^{1/2} \left[1 + 2\sum_{1}^{\infty} (-1)^n exp\left(\frac{-n^2 d^2}{Dt}\right) \right]$$
 (3)

, where q (Pa.m³)/(m².s) is the outgassing rate, D (m²/s) is the diffusion coefficient, C_0 (Pa) is the pressure of gas molecules inside the wall, and 2d is wall thickness [25]. Equations 4 and 5 are followed from Equation 3 when t approaches zero and infinity, respectively.

$$q_{@t=0} = C_0 \left(\frac{D}{\pi t}\right)^{1/2} \tag{4}$$

$$q_{@t=\infty} = \frac{2DC_0}{d} exp\left(-\frac{\pi^2 Dt}{4D^2}\right)$$
 (5)

These equations show that initially diffusion (of nearsurface molecules to the surface), which is usually a slower process than desorption, governs the outgassing kinetics. However, after very long time the slow desorption of the last monolayer is the rate determining factor.

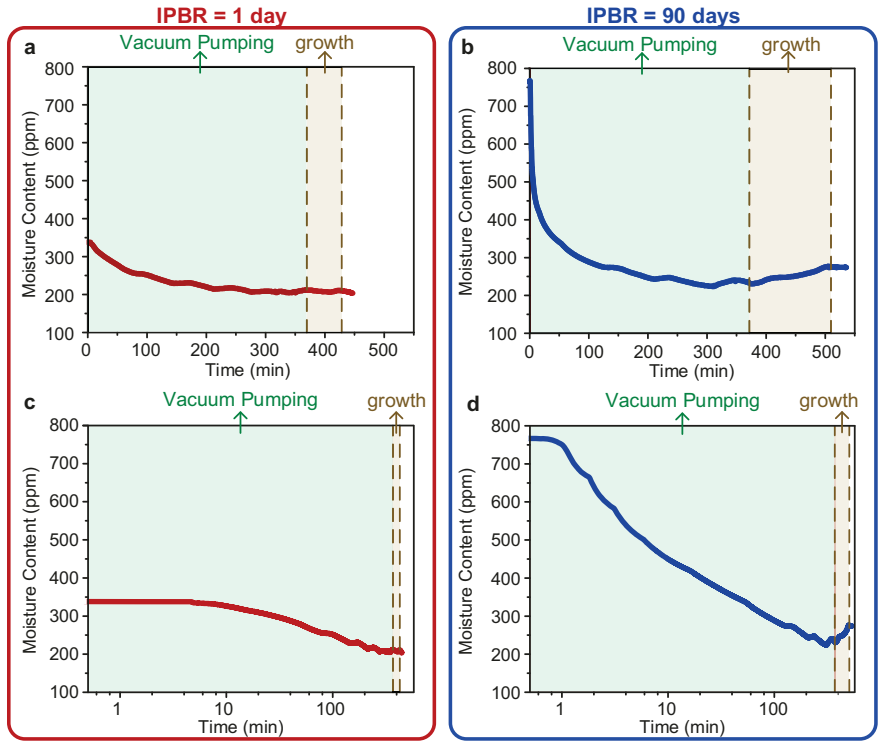


FIGURE 7: Variation in moisture content during the growth recipe for two forests with 1-day IPBR (a, c) and 90-day IPBR (b, d).

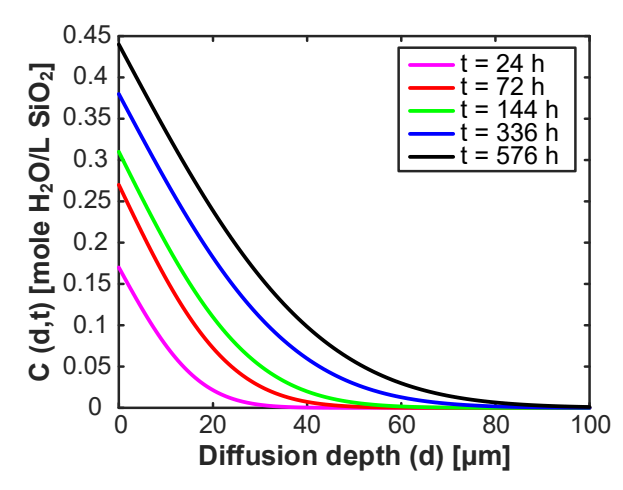


FIGURE 8: Concentration depth profiles at various exposure times based on Equation 1 and the experimental data from [33].

We used Equation 3 with the diffusion depths (d_1 and d_2), $C_{avg,1}$ and $C_{avg,2}$, and $D=10^{-18}$ m².s⁻¹ to plot the outgassing rate during growths with 1-day and 90-day IPBR. It should be noted that the unit of C_{avg} was converted from mole/L of SiO₂ to Pa by using the density of silica glass to calculate the molar ratio of water vapor molecules in one liter of SiO₂ and convert it to partial pressure in Pa. We obtained 6.76 x 10³ Pa and 2.30 x 10⁴ Pa for the 1-day and 90-day IPBR, respectively. The semilogarithmic plots in Fig. 10c demonstrate noticeably higher outgassing rate for the case with 90-day IPBR. Additionally, the log-log plot in Fig. 10d shows that the transition time, at which the outgassing rate changes from diffusion-limited to desorption-limited, shifts to higher values in the case of 90-day IPBR.

These findings confirm that extended IPBR leads to higher outgassing rates over a longer period of time. This is in agreement with our experimental CNT forest characterization results, as well as the real-time humidity measurements. Taken together, the modeling results and the experimental findings provide strong evidence that higher amounts of water vapor molecules outgas from the reactor walls and enter the reactor during growth after extended IPBR. While these growthpromoting molecules can increase the yield of CNTs, the uncontrolled release of them during the growth process leads to run-to-run variations and nonuniform geometry and properties of the forests. Hence, our study paves the way for leveraging this phenomenon by creating new reactor conditioning steps to tune the amount of gas molecules outgassing from the reactor walls during growth. These conditioning steps could be either added during the IPBR or added to the growth recipe. For example, temperature and pressure control, as well as gas flow during the IPBR can enable creating more scalable and robust manufacturing processes for CNTs by CVD. Also, we envision adding shorter steps before growth to create conditions equivalent to having extended IPBR. For example, we can introduce water vapor at higher temperatures followed by roomtemperature vacuum pumping, considering that adsorption can be more favorable than degassing [25]. We can also use a similar

strategy to saturate a fused silica wafer with water vapor and place it in the reactor as the substrate holder during growth.

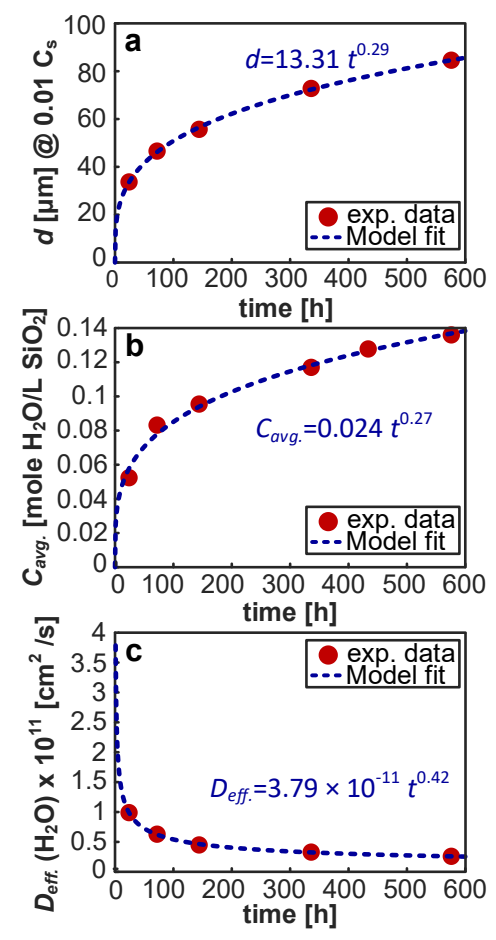


FIGURE 9: Time dependence of (a) diffusion depth at concentration 0.01 C_s , (b) Average concentration within this diffusion depth, and (c) effective diffusion coefficient of water molecules into silica glass. The experimental data is based on the results from [33]. Dashed blue lines are power law models that best fits the data.

4. CONCLUSION

A systematic study on the effect of the thermochemical history of reactor wall on CNT forest growth is required in order to both greatly enhance the yield and reduce run-to-run variations. Here we used both experimental measurements and mathematical modeling to investigate the effect of interim period between growth runs (IPBR) on the growth and properties of CNT forests. Our results demonstrate that increasing the IPBR increases the CNT yield, resulting in almost one order of magnitude increase in catalytic lifetime, while impacts growth reproducibility. Our modeling results show that increasing IPBR greatly boosts the kinetics of outgassing, which acts as a continuous supply of growth-promoting molecules. Additionally, the newly installed humidity sensor enabled us to correlate the moisture content with the growth dynamics of CNT forests and their yield. Therefore, higher amounts of water vapor molecules that are adsorbed and diffuse into the reactor wall during extended IPBR can be leveraged as the underlying mechanism behind a new approach to grow CNTs with unexpectedly high yields.

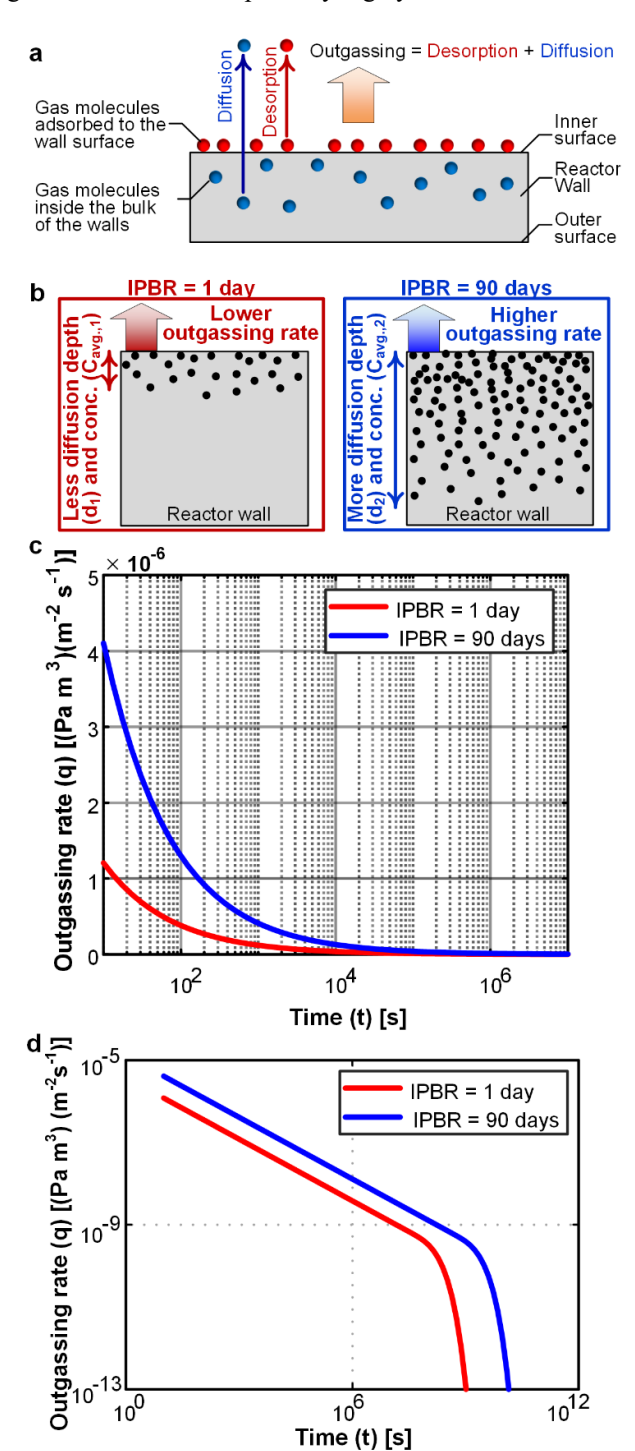


FIGURE 10: (a) Schematic representation of diffusion of H₂O molecules from within the reactor wall to the surface and desorption from the surface as the two major contributors to the outgassing. (b) Schematic illustration of the effect of IPBR on diffusion depth and the amount of water vapor molecules that diffuse into the reactor walls (concentration). (c,d) Effect of IPBR on outgassing rate, as semilog plot (c) and log-log plot (d).

ACKNOWLEDGEMENTS

This research was supported by the National Science Foundation (Award Number: 1825772) and the Department of Industrial Engineering at the University of Pittsburgh. Sample preparation and characterization were performed, in part, at the Nanoscale Fabrication and Characterization Facility, a laboratory of the Gertrude E. and John M. Petersen Institute of NanoScience and Engineering, housed at the University of Pittsburgh.

REFERENCES

- [1] Tong, T., Zhao, Y., Delzeit, L., Kashani, A., Meyyappan, M., and Majumdar, A., 2007, "Dense Vertically Aligned Multiwalled Carbon Nanotube Arrays as Thermal Interface Materials," IEEE Trans. Components Packag. Technol., 30(1), pp. 92–100.
- [2] Majumder, M., Chopra, N., Andrews, R., and Hinds, B. J., 2005, "Enhanced Flow in Carbon Nanotubes," Nature, 438(7064), pp. 44–44.
- [3] Wei, B. Q., Vajtai, R., and Ajayan, P. M., 2001, "Reliability and Current Carrying Capacity of Carbon Nanotubes," Appl. Phys. Lett., **79**(8), pp. 1172–1174.
- [4] Liang, X., Shin, J., Magagnosc, D., Jiang, Y., Jin Park,
 S., John Hart, A., Turner, K., Gianola, D. S., and Purohit,
 P. K., 2017, "Compression and Recovery of Carbon Nanotube Forests Described as a Phase Transition," Int.
 J. Solids Struct., 122–123, pp. 196–209.
- [5] Bedewy, M., 2017, "Data-Driven Understanding of Collective Carbon Nanotube Growth by in Situ Characterization and Nanoscale Metrology," J. Mater. Res., **32**(01), pp. 153–165.
- [6] Bedewy, M., Meshot, E. R., Guo, H., Verploegen, E. A., Lu, W., and Hart, A. J. J., 2009, "Collective Mechanism for the Evolution and Self-Termination of Vertically Aligned Carbon Nanotube Growth," J. Phys. Chem. C, 113(48), pp. 20576–20582.
- [7] Bedewy, M., Meshot, E. R., Reinker, M. J., and Hart, A. J., 2011, "Population Growth Dynamics of Carbon Nanotubes," ACS Nano, 5(11), pp. 8974–8989.
- [8] Bedewy, M., Viswanath, B., Meshot, E. R., Zakharov, D. N., Stach, E. A., and Hart, A. J., 2016, "Measurement of the Dewetting, Nucleation, and Deactivation Kinetics of Carbon Nanotube Population Growth by Environmental Transmission Electron Microscopy," Chem. Mater., 28(11), pp. 3804–3813.
- [9] Balakrishnan, V., Bedewy, M., Meshot, E. R., Pattinson, S. W., Polsen, E. S., Laye, F., Zakharov, D. N., Stach, E. A., and Hart, A. J., 2016, "Real-Time Imaging of Self-Organization and Mechanical Competition in Carbon Nanotube Forest Growth," ACS Nano, 10(12), pp. 11496–11504.
- [10] Tsentalovich, D. E., Headrick, R. J., Mirri, F., Hao, J., Behabtu, N., Young, C. C., and Pasquali, M., 2017, "Influence of Carbon Nanotube Characteristics on Macroscopic Fiber Properties," ACS Appl. Mater. Interfaces, 9(41), pp. 36189–36198.
- [11] Hata, K., Futaba, D. N., Mizuno, K., Namai, T., Yumura,

- M., and Iijima, S., 2004, "Water-Assisted Highly Efficient Synthesis of Impurity-Free Single-Walled Carbon Nanotubes," Science (80-.)., **306**(5700), pp. 1362–1364.
- [12] Arcila-Velez, M. R., Zhu, J., Childress, A., Karakaya, M., Podila, R., Rao, A. M., and Roberts, M. E., 2014, "Roll-to-Roll Synthesis of Vertically Aligned Carbon Nanotube Electrodes for Electrical Double Layer Capacitors," Nano Energy, 8, pp. 9–16.
- [13] Lee, C. H., Lee, J., Park, J., Lee, E., Kim, S. M., and Lee, K. H., 2019, "Rationally Designed Catalyst Layer toward 'Immortal' Growth of Carbon Nanotube Forest: Fe Ion Implanted Substrates," Carbon N. Y., 152, pp. 482–488
- [14] Lee, J., Tomaraei, G. N., Abdulhafez, M., and Bedewy, M., 2021, "Boosting Catalytic Lifetime in Chemical Vapor Deposition of Carbon Nanotubes by Rapid Thermal Pretreatment of Alumina-Supported Metal Nanocatalysts," Chem. Mater., 33(16), pp. 6277–6289.
- [15] Dee, N. T., Li, J., Orbaek White, A., Jacob, C., Shi, W., Kidambi, P. R., Cui, K., Zakharov, D. N., Janković, N. Z., Bedewy, M., Chazot, C. A. C., Carpena-Núñez, J., Maruyama, B., Stach, E. A., Plata, D. L., and Hart, A. J., 2019, "Carbon-Assisted Catalyst Pretreatment Enables Straightforward Synthesis of High-Density Carbon Nanotube Forests," Carbon N. Y., 153, pp. 196–205.
- [16] Plata, D. L., Hart, A. J., Reddy, C. M., and Gschwend, P. M., 2009, "Early Evaluation of Potential Environmental Impacts of Carbon Nanotube Synthesis by Chemical Vapor Deposition," Environ. Sci. Technol., 43(21), pp. 8367–8373.
- [17] Lee, J., Abdulhafez, M., and Bedewy, M., 2019, "Data Analytics Enables Significant Improvement of Robustness in Chemical Vapor Deposition of Carbon Nanotubes Based on Vacuum Baking," Ind. Eng. Chem. Res., 58(27), pp. 11999–12009.
- [18] Oliver, C. R., Polsen, E. S., Meshot, E. R., Tawfick, S., Park, S. J., Bedewy, M., and Hart, A. J., 2013, "Statistical Analysis of Variation in Laboratory Growth of Carbon Nanotube Forests and Recommendations for Improved Consistency," ACS Nano, 7(4), pp. 3565–3580.
- [19] Li, J., Bedewy, M., White, A. O., Polsen, E. S., Tawfick, S., and John Hart, A., 2016, "Highly Consistent Atmospheric Pressure Synthesis of Carbon Nanotube Forests by Mitigation of Moisture Transients," J. Phys. Chem. C, **120**(20), p. 11277–11287.
- [20] Shi, W., Li, J., Polsen, E. S., Oliver, C. R., Zhao, Y., Meshot, E. R., Barclay, M., Fairbrother, D. H., Hart, A. J., and Plata, D. L., 2017, "Oxygen-Promoted Catalyst Sintering Influences Number Density, Alignment, and Wall Number of Vertically Aligned Carbon Nanotubes," Nanoscale, 9, pp. 5222–5233.
- [21] Tomaraei, G., Abdulhafez, M., Lee, J., and Bedewy, M., 2020, "Reducing Variability in Chemical Vapor Deposition of Carbon Nanotubes Based on Gas Purification and Sample Support Redesign,"

- Proceedings of the ASME 2020 15th International Manufacturing Science and Engineering Conference MSEC2020 June 22-26, 2020, Cincinnati, OH, USA, pp. 1–10.
- [22] Liu, K., Liu, P., Jiang, K., and Fan, S., 2007, "Effect of Carbon Deposits on the Reactor Wall during the Growth of Multi-Walled Carbon Nanotube Arrays," Carbon N. Y., **45**(12), pp. 2379–2387.
- [23] Abdulhafez, M., Lee, J., and Bedewy, M., 2020, "In Situ Measurement of Carbon Nanotube Growth Kinetics in a Rapid Thermal Chemical Vapor Deposition Reactor With Multizone Infrared Heating," J. Micro Nano-Manufacturing, **8**(1).
- [24] Lee, J., Abdulhafez, M., and Bedewy, M., 2019, "Multizone Rapid Thermal Processing to Overcome Challenges in Carbon Nanotube Manufacturing by Chemical Vapor Deposition," J. Manuf. Sci. Eng., 141(9).
- [25] O'Hanlon, J. F., 2003, A User's Guide to Vacuum Techolonogy, John Wiley & Sons, Inc., Hoboken, NJ, USA.
- [26] Bedewy, M., Farmer, B., and Hart, A. J., 2014, "Synergetic Chemical Coupling Controls the Uniformity of Carbon Nanotube Microstructure Growth," ACS Nano, 8(6), pp. 5799–5812.
- [27] Bedewy, M., and Hart, A. J., 2013, "Mechanical Coupling Limits the Density and Quality of Self-Organized Carbon Nanotube Growth," Nanoscale, **5**(7), p. 2928.
- [28] Han, J. H., Graff, R. A., Welch, B., Marsh, C. P., Franks, R., and Strano, M. S., 2008, "A Mechanochemical Model of Growth Termination in Vertical Carbon Nanotube Forests," ACS Nano, 2(1), pp. 53–60.
- [29] Hajilounezhad, T., Ajiboye, D. M., and Maschmann, M. R., 2019, "Evaluating the Forces Generated during Carbon Nanotube Forest Growth and Self-Assembly," Materialia, 7(June), p. 100371.
- [30] Ago, H., Uehara, N., Yoshihara, N., Tsuji, M., Yumura, M., Tomonaga, N., and Setoguchi, T., 2006, "Gas Analysis of the CVD Process for High Yield Growth of Carbon Nanotubes over Metal-Supported Catalysts," Carbon N. Y., 44(14), pp. 2912–2918.
- [31] Yasuda, S., Hiraoka, T., Futaba, D. N., Yamada, T., Yumura, M., and Hata, K., 2009, "Existence and Kinetics of Graphitic Carbonaceous Impurities in Carbon Nanotube Forests to Assess the Absolute Purity," Nano Lett., 9(2), pp. 769–773.
- [32] Doremus, R., 1995, "Diffusion of Water in Silica Glass," J. Mater. Res., **10**(9), pp. 2379–2389.
- [33] Oehler, A., and Tomozawa, M., 2004, "Water Diffusion into Silica Glass at a Low Temperature under High Water Vapor Pressure," J. Non. Cryst. Solids, **347**(1–3), pp. 211–219.